Decoding the Promotional Effect of Iron in Bimetallic Pt-Fe-Nanoparticles for the Low Temperature Reverse Water-Gas Shift Reaction

Colin Hansen[a], Wei Zhou[a,*], Enzo Brack[a], Yuhao Wang[b], Chunliang Wang[b], James Paterson[c], Jamie Southouse[c] and Christophe Copéret[a,*]

[a] Department of Chemistry and Applied Biosciences, ETH Zürich, Vladimir Prelog Weg 1-5, CH-8093 Zurich, Switzerland

[b] Engineering Research Center of Metallurgical Energy Conservation and Emission Reduction, Ministry of Education, Kunming University of Science and Technology, Kunming 650093, China

[c] bp Technology, Applied Sciences bp plc Saltend, Hull HU12 8DS, United Kingdom

*Corresponding Authors: weizhou@ethz.ch, ccoperet@ethz.ch

ABSTRACT: The reverse water-gas shift reaction (RWGS) is a key technology of the chemical industry, central to the emerging circular carbon economy. Pt-based catalysts have previously been shown to effectively promote the RWGS, especially when modified by promoter elements. However, their active state is still poorly understood. Here, we show that the intimate incorporation of an iron promoter into metal-oxide supported Pt-based nanoparticles can increase their activity and selectivity for the low temperature reverse water-gas shift (LT-RWGS) substantially and drastically outperform unpromoted Pt-based materials. Specifically, the study explores the promotional effect of iron in Pt-Fe bimetallic systems supported on silica ($Pt_xFe_y@SiO_2$) prepared by surface organometallic chemistry (SOMC). The most active catalyst ($Pt_1Fe_1@SiO_2$) shows high selectivity (>99% CO) towards CO at a formation rate of 0.192 $mol_{CO}\ h^{-1}\ g_{cat}^{-1}$, which is significantly higher than that of monometallic $Pt@SiO_2$ (96% sel. and 0.022 $mol_{CO}\ h^{-1}\ g_{cat}^{-1}$). In-situ diffuse reflectance FT-IR spectroscopy (DRIFTS) and X-ray absorption spectroscopy (XAS) indicate a dynamic process at the catalyst surface under reaction conditions, revealing distinct reaction pathways for the monometallic $Pt@SiO_2$ and bimetallic $Pt_xFe_y@SiO_2$ systems.

INTRODUCTION

The reverse water-gas shift (RWGS)[1-4] and its corresponding reverse reaction (WGS) are key technologies because of their central role in syngas conversion in the chemical industry. Furthermore, RWGS and WGS processes are foreseen to play a major role in all processes related to CO_2 conversion and H_2 production, which are central to possible strategies for the mitigation of CO_2 emissions. Indeed, the RWGS reaction enables the conversion of CO_2 into syngas ($CO + H_2$), which can be further converted into value-added chemicals via Fischer-Tropsch synthesis and other syngas processes, e.g. methanol synthesis.[5-8] RWGS is endothermic (ΔH^0 = +42.1 kJ/mol) and thermodynamically favored at high operating temperatures (500-700 °C). However, these harsh conditions result in catalyst deactivation and high energetic cost. Therefore, current research strives to develop RWGS catalysts that can operate at moderate reaction tem-

peratures (300-500°C) with the goal to improve the productivity of the reaction and process intensification. Among reported catalytic systems, promoted platinum-based catalysts, supported on metal-oxides, have gained attention for the low-temperature RWGS (LT-RWGS).[9-13]

In that context, while Fe has attracted great interest as a promoter, due to its high natural abundance and low cost, its promotional role has remained elusive.[14] In fact, two types of RWGS mechanisms are typically proposed (**Figure 1**, Figure S 2), differing by the elementary steps associated with CO_2 activation.[1, 9, 15, 16] On the one hand, hydrogen-mediated activation of CO_2 involves the generation of hydroxycarbonyls which then decompose to yield CO; on the other hand, redox-mechanisms involve a reduced form of the promoter or support (P) to activate and convert CO_2 directly into CO, leaving an oxidized species (i.e. P(O)), which is then re-reduced to its initial reactive state by H_2.[14]

In order to gain a deeper understanding of the promotional effect of Fe in the RWGS mechanism, catalytic materials with tailored nanoparticle-support interfaces and composition (e.g. Pt-Fe alloys) are essential. While the preparation of supported nanoparticles often involves precipitation or impregnation methods in water,[17] these apparently simple processes yield complex materials and ill-defined systems,[18] which are difficult to characterize, thereby rendering the identification of structure-reactivity relationships challenging.

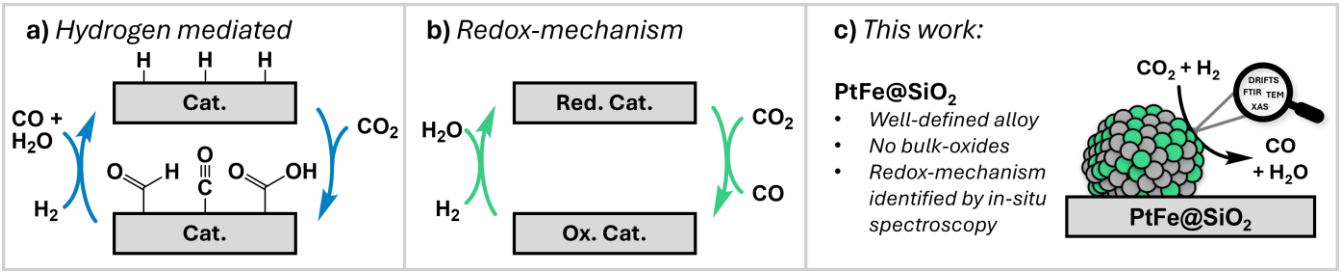

Figure 1. a) Hydrogen mediated mechanisms of RWGS involve the formation of meta-stable, carbon-containing intermediates, which decompose to form CO and H_2O; b) Redox mechanisms involve a reducible promoter (e.g. TiO_2, CeO_2 or Fe_2O_3) which can reductively activate CO_2 to form CO. Any oxidized material is subsequently re-reduced by H_2 to form water. [1, 9, 15, 16]; c) Aim of the presented work: investigation of well-defined $PtFe@SiO_2$ systems by in-situ spectroscopy under RWGS.

Here, we use Surface Organometallic Chemistry (SOMC)[19-22] to prepare well-defined, silica-supported Pt-Fe bimetallic catalysts ($Pt_xFe_y@SiO_2$) by a sequential-grafting approach.[23, 24] This approach, which is carried out in the absence of water in the preparative steps, helps to avoid dissolution-precipitation events that are known to contribute to the complexity of the resulting materials. Furthermore, this approach is readily aimable to detailed characterization. A combination of Fourier-transform infrared spectroscopy (FT-IR), elemental analysis (EA), and high-angle annular dark-field scanning transmission electron mi-

croscopy (HAADF-STEM) are used to highlight specific structural features of the materials. X-ray Absorption spectroscopy (XAS) is used to trace the chemical state of the material (surface) throughout catalysis, showing in this study the formation of bulk Pt-Fe alloys. Furthermore, in-situ diffuse reflectance FT-IR spectroscopy (DRIFTS)[25] coupled with gas-switching experiments enables the observation of subtle changes in the chemical state and environment of surface Pt, highlighting an alloying-dealloying process, consistent with a redox mechanism for the conversion of CO_2 into CO in the presence of Fe (**Figure 1**c).

RESULTS AND DISCUSSION

First, a series of Pt-Fe catalysts are synthesized by sequential grafting of two molecular precursors, Fe_2Mes_4 (Mes = Mesityl)[26] and $Pt(C_3H_5)(DIA)$ ($C_3H_5 = \eta^3$-allyl, DIA = N,N'-diisopropylacetimidinate),[27] onto a silica partially dehydroxylated at 700°C ($SiO_{2\text{-}700}$, 0.9 -OH nm^{-2}). The resulting materials contain two metal surface species (**Figure 2**a-b), for which the Pt/Fe-ratios ($\chi_{Pt/Fe}$) can be tuned at the grafting step, by choosing an adequate stoichiometry between the precursors and the surface -OH density. A subsequent treatment under H_2 flow at 600°C (ramp: 1°C min^{-1}) yields a series of supported nanoparticles (*vide infra*), coined $Pt_xFe_y@SiO_2$ (**Figure 2**c). By this approach, bimetallic materials with different $\chi_{Pt/Fe}$ are produced along with monometallic $Pt@SiO_2$ and $Fe@SiO_2$ systems. The metal loadings in all catalysts are determined by inductively coupled plasma optical emission spectroscopy (ICP-OES), revealing Pt/Fe ratios ranging between $0.22 < \chi_{Pt/Fe} < 3.23$ in bimetallic systems (**Table 1**).

Monitoring the synthetic steps via IR-spectroscopy (See **Figure 2**d for representative spectra of $Pt_1Fe_1@SiO_2$, Figure S 13-19) shows that grafting with a sub-stoichiometric amount of Fe_2Mes_4 (covering approx. 50% of the surface -OH groups) leads to a partial decrease of the ν(O-H) intensity (by ca. half), while aliphatic and aromatic C-H stretching vibrations appear. The subsequent grafting of $Pt(C_3H_5)(DIA)$ onto the residual silanol groups shows further loss of the ν(O-H) signal alongside the appearance of the typical features of a grafted imidinate complex.[27] Notably, upon hydrogen treatment, all organic ligands are removed and yield black solids. Note that some silane species associated with a ν(Si-H) at 2288 cm^{-1} are formed, indicating a partial reduction of the support under H_2.[28, 29] Such a phenomenon is typically not observed for other promoters like Mn, Zn or Ga, indicating the specific redox-ability of Fe.

All materials are also characterized by HAADF-STEM that shows narrowly distributed nanoparticles, whose size depends on $\chi_{Pt/Fe}$. While monometallic $Pt@SiO_2$ and $Fe@SiO_2$ present particles of 1.8 ± 1.0 nm and 1.5± 0.2 nm respectively, the combination of iron and platinum generally yields smaller nanoparticles (**Table 1**). For instance, $Pt_1Fe_1@SiO_2$ shows a PSD of 0.7 ± 0.2 nm, indicating a strong interaction between Pt and the Fe promoter. For sufficiently large particles, energy dispersive X-ray spectroscopy (EDX) maps show that Pt and Fe profiles strongly overlap, suggesting the formation of Pt-Fe alloys upon H_2 reduction (Figure S 37-38). The formation of an alloy is further corroborated by XAS (*vide infra*) and

high-resolution TEM images with lattice spacings consistent with the formation of PtFe alloys, *e.g.* $Pt_2Fe_1@SiO_2$ (0.21 nm) vs. Pt_3Fe_1 bulk-alloy (0.215 nm) and pure-FCC Pt (0.226 nm) (Figure S 39).

Table 1. Physical properties for all synthesized materials.

Material	Pt wt%[a]	Fe wt%[a]	$\chi_{Pt/Fe}$[b]	PSD[c] [nm]
$Pt@SiO_2$	3.96	-	-	1.8 ± 1.0
$Pt_4Fe_1@SiO_2$	4.06	0.36	3.23	1.2 ± 0.5
$Pt_2Fe_1@SiO_2$	3.97	0.64	1.78	1.5 ± 0.9
$Pt_1Fe_1@SiO_2$	3.95	1.36	0.83	0.7 ± 0.2
$Pt_1Fe_2@SiO_2$	2.39	1.52	0.45	0.7 ± 0.1
$Pt_1Fe_4@SiO_2$	1.16	1.51	0.22	-
$Fe@SiO_2$	-	1.50[d]	-	1.5 ± 0.2

[a] Metal weight loading determined by ICP-OES; [b] molar Pt/Fe ratio based on weight loadings; [c] particle size distribution (Nanoparticle counts for $Pt_1Fe_4@SiO_2$ were not possible due to low contrast, see Figure S 36); [d] weight loading of $Fe@SiO_2$ estimated from ^{1}H-NMR (SI S2.2)

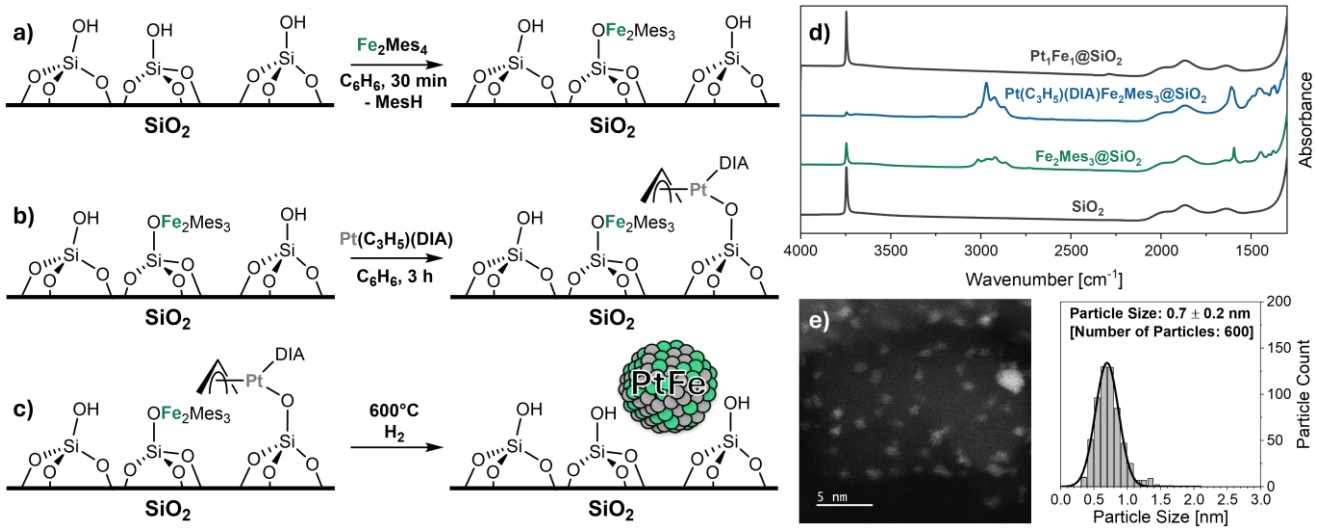

Figure 2. (a-c) Synthesis of $Pt_xFe_y@SiO_2$ by sequential grafting; (d) FT-IR Spectra of $Pt_1Fe_1@SiO_2$ in preparation; (e) HAADF-STEM image of $Pt_1Fe_1@SiO_2$ and respective particle size distribution (Scalebar: 5 nm, PSD: 0.7 ± 0.2 nm, N = 600).

In fact, IR-spectra of the samples exposed to CO show a significant red-shift and broadening of the spectroscopic features, when comparing $Pt_xFe_y@SiO_2$ to $Pt@SiO_2$, further supporting Pt-Fe alloy formation (Figure S 20-26). The occurrence of pressure dependent features at 2005 cm^{-1} and 2025 cm^{-1} hints towards the formation of a $Fe_x(CO)_y$ species, therefore indicating the presence of reduced iron.[30] The extent of the red-shift and the amount of $Fe_x(CO)_y$ species increases with increasing Fe-content (Figure S 28) and is affected by temperature.[30]

Next, the catalytic performances of both mono- and bimetallic catalysts are evaluated in LT-RWGS conditions (3:1:1 H_2/CO_2/Ar, 1 bar, 200-450°C) (SI S3.5). $Pt_1Fe_1@SiO_2$ shows the highest activity, reaching

44% CO_2 conversion at 450°C with nearly ideal CO selectivity (>99.5%); followed by $Pt_1Fe_2@SiO_2$, $Pt_4Fe_1@SiO_2$, $Pt_2Fe_1@SiO_2$ and $Pt_1Fe_4@SiO_2$, with conversions of 42%, 39%, 34% and 32%, respectively (**Figure 3**a). Due to the endothermic nature of the RWGS, the activity of all materials increases significantly upon raising the temperature. Notably, under these conditions, the most active catalyst ($Pt_1Fe_1@SiO_2$) enables near equilibrium conversion at a relatively low temperature of 400°C. In contrast, $Pt@SiO_2$ displays a significantly lower activity (10% conversion at 450°C under the same conditions), while the monometallic Fe-system shows little to no activity, thus clearly illustrating the synergy between Fe and Pt in the series of catalysts.

Besides CO, CH_4 is the only detected side-product of the reaction. Increasing the $\chi_{Pt/Fe}$ ratio leads to a decrease in CO-selectivity. $Pt_1Fe_1@SiO_2$, $Pt_1Fe_2@SiO_2$ and $Pt_1Fe_4@SiO_2$ produce practically no methane with up to 99.9% CO selectivity (**Figure 3**b). The selectivity decreases for Pt-rich catalysts to approx. 99% for $Pt_4Fe_1@SiO_2$ while the selectivity is below 96% for pure $Pt@SiO_2$. The CO formation rate per gram of catalyst (at similar Pt loading) reaches 0.192 $mol_{CO}\ h^{-1}\ g_{cat}^{-1}$ at 400°C for $Pt_1Fe_1@SiO_2$, (**Figure 3**c) which is ca. 1 order of magnitude higher than for the monometallic $Pt@SiO_2$ catalyst (0.022 $mol_{CO}\ h^{-1}\ g_{cat}^{-1}$) with $Fe@SiO_2$ being hardly active (0.006 $mol_{CO}\ h^{-1}\ g_{cat}^{-1}$). When comparing the catalysts in terms of their CO formation rates per gram catalyst, the rate reaches a maximum for a $\chi_{Pt/Fe}$ of 0.5-1.0 ($Pt_1Fe_1@SiO_2$). The formation rates normalized to Pt can reach up to ca. 1920 $mol_{CO}\ h^{-1}\ mol_{Pt}^{-1}$ at 400°C (Figure S 56). This maximum value is reached for $Pt_1Fe_4@SiO_2$, likely pointing out that smaller particles, and therefore increased metal-dispersion, increase the number of active sites. Finally, a stability test shows only a small deactivation of the catalyst over time in LT-RWGS at 400°C for $Pt_1Fe_1@SiO_2$, with 90% of the initial activity after 45h (Figure S 54).

A contact time study on $PtFe@SiO_2$ (Figure S 52) shows a flattening of the activity curve for increasing contact times, as the conversion reaches thermodynamic equilibrium, consistent with saturation kinetics. Also note the increased methane selectivity (from <0.1% to ca. 0.4% CH_4-selectivity) at longer contact times, evidencing the competitive Sabatier or CO methanation reactions (Figure S 55).

Notably, the apparent activation energies (E_A) for the overall RWGS process, measured for all Pt-catalysts in the temperature range of 200 to 350°C (**Figure 3**d and Figure S 57), vary as a function of $\chi_{Pt/Fe}$: it is the lowest for $Pt_1Fe_1@SiO_2$ at 53.2 ± 1.3 kJ/mol, while the monometallic $Pt@SiO_2$ and $Fe@SiO_2$ systems have significantly higher E_A of 64.7 ± 1.0 and 62.3 ± 1.7 kJ/mol, respectively. The obtained E_A are comparable to what was reported for related Pt-Fe containing systems on CeO_2.[10]

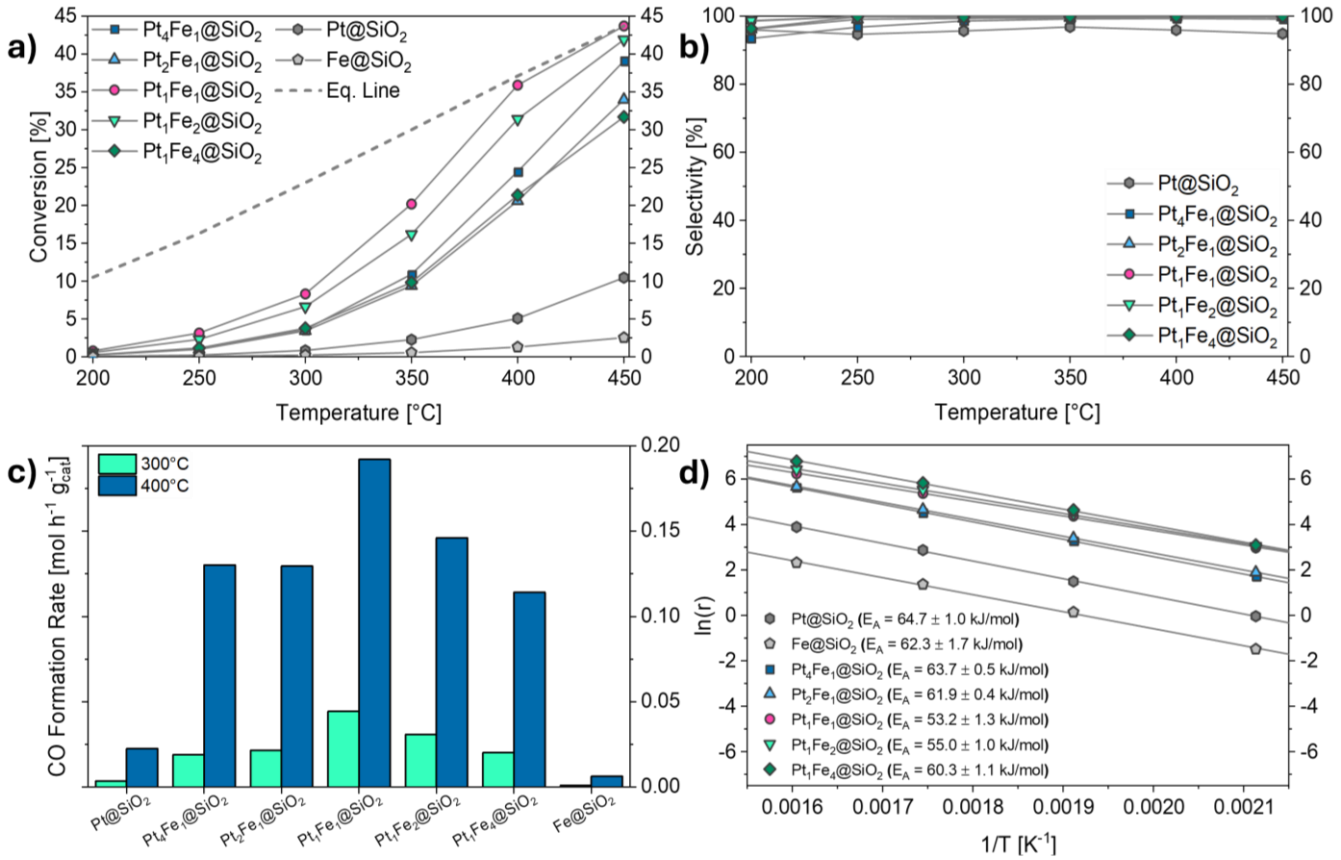

Figure 3. (a) CO_2 conversion at various temperatures for the monometallic ($Pt@SiO_2$ and $Fe@SiO_2$) and bimetallic ($Pt_xFe_y@SiO_2$) systems (Conditions: 20 mL min^{-1} (1:3:1 $CO_2/H_2/Ar$) at 1bar and 200-450 °C), Catalyst amount: 20 mg diluted in 2g SiC; (b) CO selectivities of all catalysts during LT-RWGS; (c) CO formation rates in $mol_{CO}\ h^{-1}\ g_{cat}^{-1}$ at 300 and 400°C; (d) Linear regression analysis according to Arrhenius-law in the temperature regime of 200 -350°C with calculated E_A including standard error.

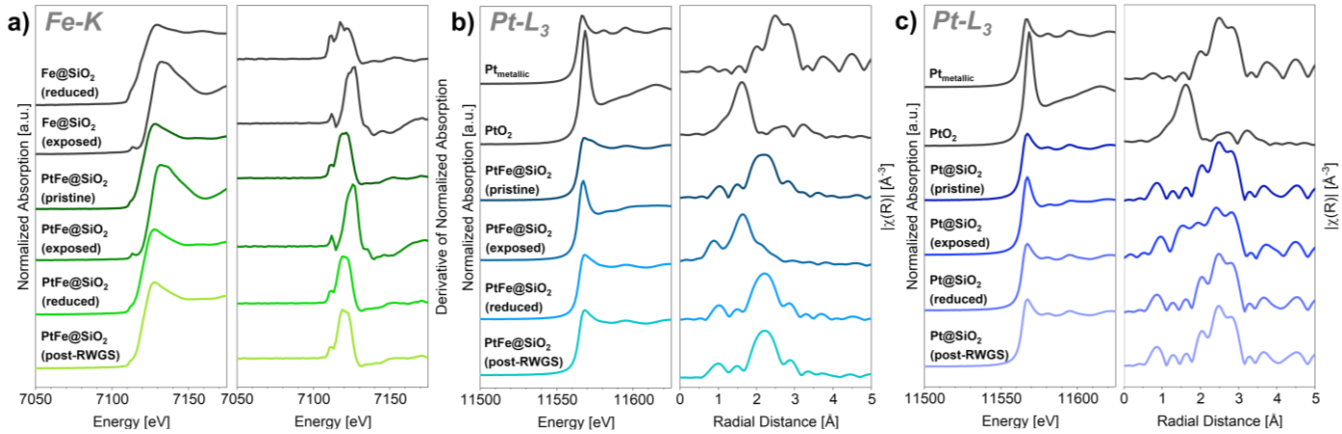

Figure 4. XANES and R-Space under various conditions (pristine, exposed, reduced, post-RWGS) for (a) $PtFe@SiO_2$ (Fe-K edge); (b) $PtFe@SiO_2$ ($Pt\text{-}L_3$ edge); (c) $Pt@SiO_2$ ($Pt\text{-}L_3$ edge).

Furthermore, one can also compare the series of catalysts considering kinetic compensation effects using a Constable plot, *i.e.* ln(A) vs. E_A (A = preexponential factor extracted from Arrhenius plots), where linear relationships can point to a physical relationship, *e.g.* similar reaction mechanisms.[31, 32] The Constable plot for our materials (Figure S 58) reveals a linear relationship between bimetallic materials, in particular when Fe-rich, while pure Pt@SiO_2 is always an outlier, indicating that monometallic and bimetallic materials operate via distinct mechanisms.

The volcano-type behaviour with an ideal composition of $0.5 < \chi_{Pt/Fe} < 1.0$ (**Figure 3**c) indicates that Pt_1Fe_1@SiO_2 (henceforth referred to as PtFe@SiO_2) displays the greatest synergistic effect between Pt and Fe. We next carried out X-Ray absorption spectroscopy (XAS) analysis of the Pt and Pt-Fe-systems at the Pt-L_3 and Fe-K edges, from the preparation step to the reaction conditions. Analysis of the pristine PtFe@SiO_2 catalyst by Fe K edge X-ray absorption near-edge structure (XANES), and comparison to Fe-foil as a standard, reveals that a large portion of iron is in a metallic state. Upon exposure to air, iron is fully oxidized (**Figure 4**a), most likely to Fe^{3+} when comparing to Fe-standards (Fe, FeO, Fe_2O_3 and Fe_2O_4, Figure S 62). Following the pre-treatment under H_2 at 400°C, the Fe K edge white line intensity decreases and the edge position shifts to lower energy (7125.9 eV to 7119.3 eV), indicating that a portion of the Fe^{3+} is readily reduced to metallic Fe^0 (Figure S 65). By comparison, the Fe K edge XANES for catalysts before and after LT-RWGS at 350°C only reveals minute changes, indicating marginal oxidation of Fe (Figure S 66) upon exposure to reaction conditions. Similarly, characterization of PtFe@SiO_2 at the Pt L_3 edge XANES also shows that ca. 38% of Pt is oxidized after exposure to air, paralleling what is observed at the Fe-edge (Figure S 67). In the subsequent H_2 pretreatment, the reduction to metallic Pt is evidenced by a decrease of the Pt L_3 edge white line intensity (**Figure 4**b). Notably, the Pt L_3 edge under RWGS at 350°C also indicates slight oxidation or dealloying of Pt (Figure S 66).

The XANES spectrum of monometallic Pt@SiO_2 upon air-exposure shows less oxidized Pt (only 25% of all Pt), as evidenced by linear combination fitting (LCF). H_2 pretreatment then causes only slight changes in white line intensity (**Figure 4**a) upon full reduction of Pt. These observations show that Pt in the monometallic system is more oxidation resistant than in the bimetallic system.

Fitting of the Pt L_3 edge Extended X-Ray absorption fine structure (EXAFS) (Figure S 68-76) of the air exposed PtFe@SiO_2 catalyst reveals the presence of Pt-O scattering paths ($CN_{Pt\text{-}O} = 2.5 \pm 0.6$), as well as low-degeneracy Pt-Pt paths ($CN_{Pt\text{-}Pt} = 3.6 \pm 2.0$) consistent with the presence of oxidised Pt^{n+} species determined by LCF. After H_2 pretreatment, no Pt-O paths can be fitted, indicating the oxidized Pt is reversibly reduced. The fitting result of the EXAFS spectrum show an average CN of 8.5 and 3.0 for Pt-Pt and Pt-Fe respectively, implying the formation of a Pt-Fe alloy after H_2 reduction, consistent with the EDX mapping and CO-IR results. Regarding the Fe-K edge, while no high-quality fittings could be obtained, the Fe K edge EXAFS of reduced PtFe@SiO_2 shows a peak at 2.5 Å, which lies between the second shell Fe-O paths of the exposed Fe@SiO_2 (mostly Fe_2O_3) and the Fe-Fe paths in reduced Fe@SiO_2

(mostly Fe^0), also hinting towards Fe-Pt scattering paths (Figure S 65). After RWGS, the Pt-Pt and Pt-Fe scattering paths remain practically unchanged ($CN_{Pt\text{-}Pt} = 9.3 \pm 2.5$, $CN_{Pt\text{-}Fe} = 3.0 \pm 1.0$).

Overall, confronting the observations at the Pt L_3 and Fe K edge shows that the change of state of both metals is strongly correlated, and the investigation of the Pt-L_3 EXAFS region (by fitting analysis) reveals the incorporation of metallic iron into Pt-based nanoparticles to form a Pt-Fe alloy. This also shows that the reduction of oxidized Fe^{n+} is possible in the presence of Pt (which has been shown to have good H_2 activation abilities).[2, 33]

Monometallic Pt@SiO_2, on the other hand, shows higher degeneracy Pt-Pt scattering paths ($CN_{Pt\text{-}Pt} = 7.1 \pm 1.6$) and lower degeneracy Pt-O paths ($CN_{Pt\text{-}Pt} = 1.6 \pm 0.7$) upon air exposure. This agrees with a higher oxidation resistance in the absence of iron. Reduction leads to the complete disappearance of Pt-O paths and an increase in path degeneracy of Pt-Pt ($CN_{Pt\text{-}Pt} = 10.5 \pm 1.2$) consistent with full reduction. RWGS again has little to no impact on the Pt-Pt path ($CN_{Pt\text{-}Pt} = 10.4 \pm 1.2$).

However, while Pt and Fe can be reversibly oxidized and reduced upon exposure to air and H_2, little changes are observed under reaction conditions according to XAS analysis. In order to gain further insight into possible changes and dynamics associated with surface sites (not readily probed by XAS), we therefore turn our attention to in-situ IR-spectroscopy. For this, the catalysts are first pretreated under H_2 at 400°C and then flushed with Ar. Then the atmosphere is switched in 30 min intervals between CO_2/Ar and H_2/Ar at 1 bar and 350°C, thus separating the reaction conditions of RWGS into oxidizing and reducing stages (See SI S1.2 for detailed procedures). The system is simultaneously examined by DRIFTS with a time resolution of 1 min.

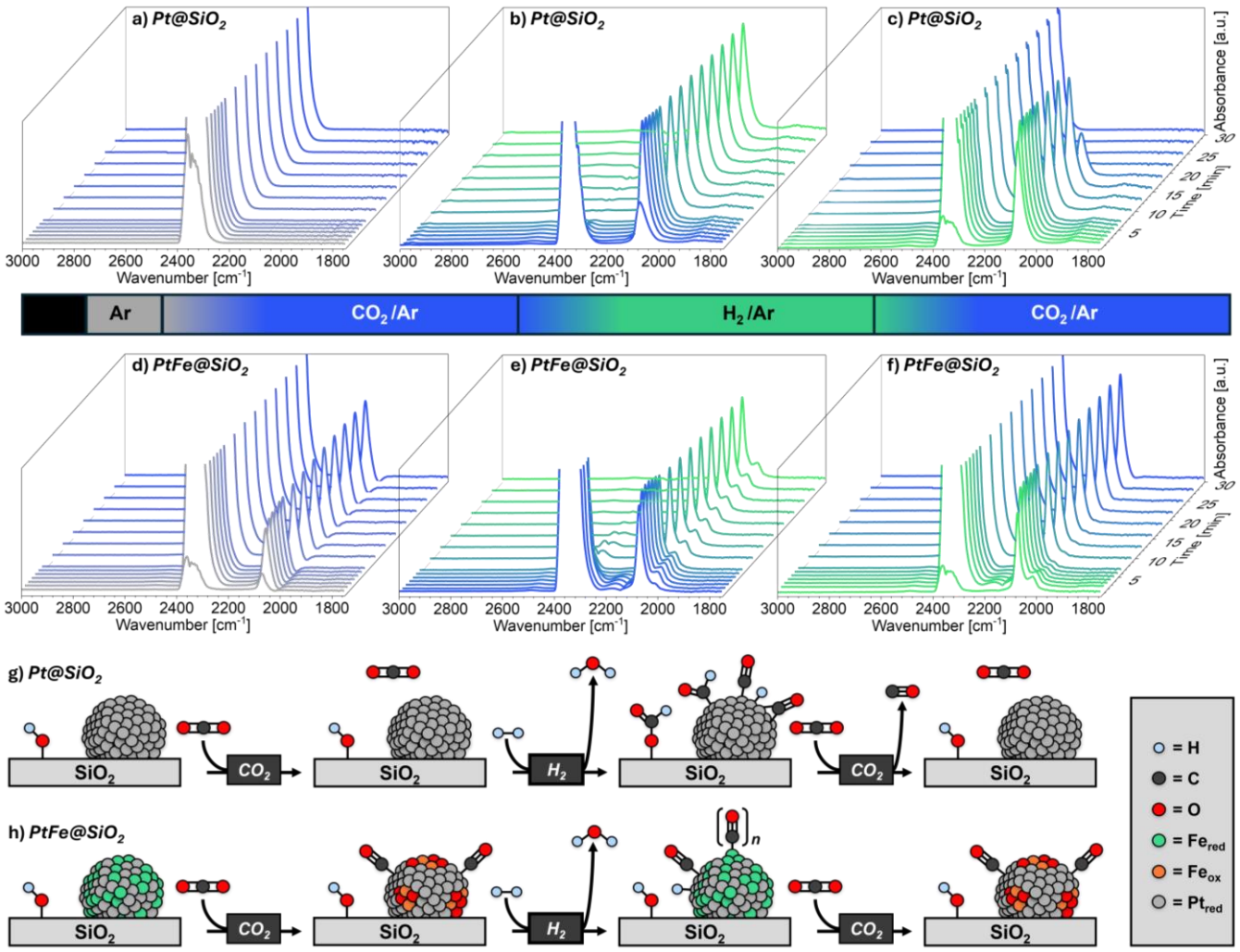

Figure 5. (d-f) In-situ DRIFTS for Pt@SiO_2 under CO_2/Ar (a) H_2/Ar (b) and CO_2/Ar (c); (d-f) In-situ DRIFTS for PtFe@SiO_2 under CO_2/Ar (d) H_2/Ar (e) and CO_2/Ar (f); (g-h) Schematic representation of distinct mechanistic pathways for Pt@SiO_2 and PtFe@SiO_2 under LT-RWGS conditions: (g) Hydrogen mediated CO_2 activation over monometallic Pt@SiO_2 (h) CO_2 activation by Fe^0-Fe^{n+} redox couple and H_2 activation by Pt in PtFe@SiO_2.

For Pt@SiO_2, the first switch to CO_2 shows only gaseous CO_2 (ca. 2350 cm^{-1}) according to IR-spectroscopy (**Figure 5**a). After switching to pure H_2 two distinct peaks of CO bound to Pt can be observed: 2070 cm^{-1} and 1859 cm^{-1} associated with terminal μ_1-CO_{ads} and weak bridging μ_2-CO_{ads}, respectively (**Figure 5**b).[34] Finally, the adsorbed CO is removed in the presence of pure CO_2 (**Figure 5**c). In addition to the strong signals described before, weak bands at 2908 and 2965 cm^{-1}, ascribed to formate species (on the support or metallic particle), can be observed under the H_2 atmosphere (Figure S 60).[35]

In sharp contrast, exposure of PtFe@SiO_2, previously treated with H_2, to a CO_2 flow shows the immediate appearance of a peak at 2070 cm^{-1} associated with CO_{ads}, besides gaseous CO_2 (**Figure 5**d). Note that no peak at 1859 cm^{-1} associated with bridging μ_2-CO_{ads} is observed, further indicating Pt and Fe remain (mostly) alloyed. Under hydrogen a third peak appears at 2013 cm^{-1} (**Figure 5**e), which can be ascribed

to the CO-stretching frequency of CO bound to metallic iron (as in $Fe(CO)_5$).[36] The emergence of this peak therefore indicates the presence of Fe^0, likely originating from the Pt-Fe alloy and possibly evidencing partial de-alloying. Switching back to CO_2 atmosphere leads to the disappearance of the shoulder at 2013 cm^{-1} but does not remove the signal at 2070 cm^{-1} (**Figure 5**f). In addition to adsorbed CO, gaseous CO can be observed at 2143 cm^{-1} (as it is being formed) during the transition period between atmospheres,[37] in line with the LT-RWGS results, where the PtFe@SiO_2 show superior CO formation rate compared to Pt@SiO_2.

Based on XAS and in-situ DRIFTS results as well as the kinetic study, we propose that Pt@SiO_2 and PtFe@SiO_2 operate via two distinct reaction mechanisms: i) for the monometallic Pt@SiO_2 the presence of both CO_2 and H_2 are required to activate CO_2 and initiate RWGS (**Figure 5**g); formate species are observed and an associative mechanism (hydrogen-mediated activation of CO_2) is most likely involved, vs. ii) for PtFe@SiO_2, *CO_2 can be activated in the absence of H_2*, which is likely due to the presence of Fe^0 species, which can reduce CO_2 to CO directly and form FeO_x (**Figure 5**h). The presence of H_2 can re-reduce the oxidized iron and enable re-alloying by the presence of platinum, thus opening the possibility to start a new turnover and RWGS catalysis. Considering that CO_2 can be converted into CO in the absence of H_2 for the bimetallic systems, the reaction over PtFe@SiO_2 likely occurs through a redox-mechanism with the involvement of a highly dynamic Fe^0-Fe^{n+} (n = 2 or 3) redox-pair in close proximity to Pt, that promote the reduction of CO_2 and the redox cycle, respectively. The redox-pair, i.e. a Fe-FeO_x interface, is not observed experimentally, likely due to a fast reduction of Fe near Pt under RWGS conditions (H_2 rich conditions). This is consistent with little to no changes in XAS throughout RWGS. This putative interface may help to open additional reaction pathways, involving carbon-containing intermediates, e.g. formates. In fact, formates are observed at 200 °C, a lower temperature at which the Pt-Fe catalysts are hardly active in RWGS (Figure S 61). This observation may indicate the occurrence of alternative pathways, particularly efficient at lower temperatures or different gas compositions. In fact, Pt-$Fe(OH)_x$ interfaces have been proposed as active sites in the preferential oxidation of CO (PROX: $CO/O_2/H_2$),[38] which is related to WGS (CO/H_2O) and involves common intermediates (hydroxy and hydroxycarbonyl).

The complete absence of platinum has detrimental effects on catalytic activity (**Figure 3**a), indicating the necessity of a metal with high H_2-affinity (such as Pt) to efficiently adsorb and activate H_2. However, we also show that the CO_2 activation capabilities of a pure Pt-based catalyst are inferior to those of a bimetallic Pt-Fe material, where Fe seems to be responsible for the activation of CO_2, while Pt activates H_2. We therefore propose that the inclusion of Fe as a promoter in the Pt-based system, and the apparent switch in reaction mechanism, is responsible for the strong promotional effect of iron in PtFe@SiO_2 and the change of E_A.

CONCLUSIONS

In summary, small, narrowly distributed, silica-supported Pt-Fe particles prepared via an SOMC approach provide highly active and stable bimetallic LT-RWGS catalysts. The CO_2 conversion over PtFe@SiO_2 with a 1:1 Pt/Fe ratio, reaches thermodynamic equilibrium at 400 °C and shows a CO formation rate of 0.19 mol_{CO} h^{-1} g_{cat}^{-1}, which is ca. 9 times higher than that of Pt@SiO_2, while Fe@SiO_2 is barely active, clearly pointing out a synergistic effect between Fe and Pt. XAS and in-situ DRIFTS highlight a complex surface chemistry that occurs with PtFe@SiO_2 systems in LT-RWGS conditions. Notably, PtFe@SiO_2 is able to reduce CO_2 in the absence of H_2, pointing towards a redox mechanism, which sharply contrasts with what is observed with pure Pt. Yet, the bulk Pt-Fe alloy formed under H_2 treatment is persistent throughout RWGS. However, our data indicate that a small portion of Fe present at the catalyst surface is involved in an alloying-de-alloying process according to in situ IR spectroscopy, likely involving fast Fe^0-Fe^{n+} redox dynamics promoted by Pt. While Pt is also responsible for the efficient activation of H_2, the redox process is crucial for the activation of CO_2. This mechanism stands in stark contrast to the hydrogen mediated mechanism of CO_2 activation proposed for monometallic Pt@SiO_2, therefore highlighting the synergy between Pt and Fe in these bimetallic catalysts.

ASSOCIATED CONTENT

Experimental procedures, purification procedures for commercial chemicals, Instrument specifications, and characterization data are covered in greater detail in the *Supporting Information*, which is provided as a separate document.

AUTHOR INFORMATION

Corresponding Authors

Wei Zhou – Department of Chemistry and Applied Biosciences, ETH Zürich, CH-8093 Zurich, Switzerland; orcid.org/0000-0002-4287-8941; Email: weizhou@ethz.ch

Christophe Copéret – Department of Chemistry and Applied Biosciences, ETH Zürich, CH-8093 Zurich, Switzerland; orcid.org/0000-0001-9660-3890; Email: ccoperet@ethz.ch

Authors

Colin Hansen – Department of Chemistry and Applied Biosciences, ETH Zürich, CH-8093 Zurich, Switzerland; orcid.org/0009-0004-0479-0430

Enzo Brack – Department of Chemistry and Applied Biosciences, ETH Zürich, CH-8093 Zurich, Switzerland; orcid.org/0000-0003-4078-3006

Yuhao Wang – Engineering Research Center of Metallurgical Energy Conservation and Emission Reduction, Ministry of Education, Kunming University of Science and Technology, Kunming 650093, China

Chunliang Wang – Engineering Research Center of Metallurgical Energy Conservation and Emission Reduction, Ministry of Education, Kunming University of Science and Technology, Kunming 650093, China

James Paterson – bp Technology, Applied Sciences bp plc Saltend, Hull HU12 8DS, United Kingdom; orcid.org/0000-0003-1016-5776

Jamie Southouse – bp Technology, Applied Sciences bp plc Saltend, Hull HU12 8DS, United Kingdom

Notes

The Authors declare no conflict of interest.

ACKNOWLEDGEMENTS

C.C. & W.Z. thank bp p.l.c. for financial support. C.C. & C.H. acknowledge the Swiss National Science Foundation SNSF Sinergia Project (grant CRSII5_216681). This publication was created as part of NCCR Catalysis (grant number 180544), a National Center of Competence in Research funded by the Swiss National Science Foundation. The Swiss Norwegian beamlines (SNBL at ESRF) are acknowledged for provision of beamtime and its staff for invaluable support. The BM31 setup was funded by the Swiss National Science Foundation (grant 206021_189629) and the Research Council of Norway (grant 296087). Furthermore, ScopeM is gratefully acknowledged for their support and assistance in this work through project No. 2568. We thank one of the reviewers for pointing out previous works related to kinetic compensation effects.

NOTES AND REFERENCES

(1) González-Castaño, M.; Dorneanu, B.; Arellano-García, H. The reverse water gas shift reaction: a process systems engineering perspective. *React. Chem. Eng.* **2021**, *6* (6), 954-976.
(2) Zhu, M.; Ge, Q.; Zhu, X. Catalytic Reduction of CO2 to CO via Reverse Water Gas Shift Reaction: Recent Advances in the Design of Active and Selective Supported Metal Catalysts. *Trans. Tianjin Univ.* **2020**, *26* (3), 172-187.
(3) Su, X.; Yang, X.; Zhao, B.; Huang, Y. Designing of highly selective and high-temperature endurable RWGS heterogeneous catalysts: recent advances and the future directions. *J. Energy Chem.* **2017**, *26* (5), 854-867.
(4) Zhang, W.; Sun, J.; Wang, H.; Cui, X. Recent Advances in Hydrogenation of CO2 to CO with Heterogeneous Catalysts Through the RWGS Reaction. *Chem. Asian J.* **2024**, *19* (4), e202300971.
(5) Zhou, W.; Cheng, K.; Kang, J.; Zhou, C.; Subramanian, V.; Zhang, Q.; Wang, Y. New horizon in C1 chemistry: breaking the selectivity limitation in transformation of syngas and hydrogenation of CO2 into hydrocarbon chemicals and fuels. *Chem. Soc. Rev.* **2019**, *48* (12), 3193-3228.
(6) Pan, X.; Jiao, F.; Miao, D.; Bao, X. Oxide–Zeolite-Based Composite Catalyst Concept That Enables Syngas Chemistry beyond Fischer–Tropsch Synthesis. *Chem. Rev.* **2021**, *121* (11), 6588-6609.
(7) Zhang, R.; Wang, Y.; Gaspard, P.; Kruse, N. The oscillating Fischer-Tropsch reaction. *Science* **2023**, *382* (6666), 99-103.
(8) Torres Galvis, H. M.; Bitter, J. H.; Khare, C. B.; Ruitenbeek, M.; Dugulan, A. I.; de Jong, K. P. Supported Iron Nanoparticles as Catalysts for Sustainable Production of Lower Olefins. *Science* **2012**, *335* (6070), 835-838.
(9) Chen, X.; Chen, Y.; Song, C.; Ji, P.; Wang, N.; Wang, W.; Cui, L. Recent Advances in Supported Metal Catalysts and Oxide Catalysts for the Reverse Water-Gas Shift Reaction. *Front Chem* **2020**, *8*, 709.
(10) Wang, H.; Bootharaju, M. S.; Kim, J. H.; Wang, Y.; Wang, K.; Zhao, M.; Zhang, R.; Xu, J.; Hyeon, T.; Wang, X.; et al. Synergistic Interactions of Neighboring Platinum and Iron Atoms Enhance Reverse Water-Gas Shift Reaction Performance. *J. Am. Chem. Soc.* **2023**, *145* (4), 2264-2270.

(11) Zhao, Z.; Wang, M.; Ma, P.; Zheng, Y.; Chen, J.; Li, H.; Zhang, X.; Zheng, K.; Kuang, Q.; Xie, Z.-X. Atomically dispersed Pt/CeO2 catalyst with superior CO selectivity in reverse water gas shift reaction. *Appl. Catal., B* **2021**, *291*, 120101.
(12) He, Y.; Huang, D. Single-Atom Platinum Catalyst for Efficient CO(2) Conversion via Reverse Water Gas Shift Reaction. *Molecules* **2023**, *28* (18), 6630.
(13) Mine, S.; Yamaguchi, T.; Ting, K. W.; Maeno, Z.; Siddiki, S. M. A. H.; Oshima, K.; Satokawa, S.; Shimizu, K.-i.; Toyao, T. Reverse water-gas shift reaction over Pt/MoOx/TiO2: reverse Mars–van Krevelen mechanism via redox of supported MoOx. *Catal. Sci. Technol.* **2021**, *11* (12), 4172-4180, 10.1039/D1CY00289A.
(14) Ruiz Puigdollers, A.; Schlexer, P.; Tosoni, S.; Pacchioni, G. Increasing Oxide Reducibility: The Role of Metal/Oxide Interfaces in the Formation of Oxygen Vacancies. *ACS Catal.* **2017**, *7* (10), 6493-6513.
(15) Yan, B.; Zhao, B.; Kattel, S.; Wu, Q.; Yao, S.; Su, D.; Chen, J. G. Tuning CO2 hydrogenation selectivity via metal-oxide interfacial sites. *J. Catal.* **2019**, *374*, 60-71.
(16) Chen, L.; Filot, I. A. W.; Hensen, E. J. M. Elucidation of the Reverse Water–Gas Shift Reaction Mechanism over an Isolated Ru Atom on CeO2(111). *J. Phys. Chem. C* **2023**, *127* (41), 20314-20324.
(17) Sietsma, J. R. A.; Jos van Dillen, A.; de Jongh, P. E.; de Jong, K. P. Application of ordered mesoporous materials as model supports to study catalyst preparation by impregnation and drying. In *Scientific Bases for the Preparation of Heterogeneous Catalysts*, Studies in Surface Science and Catalysis, 2006; pp 95-102.
(18) Munnik, P.; de Jongh, P. E.; de Jong, K. P. Recent Developments in the Synthesis of Supported Catalysts. *Chem. Rev.* **2015**, *115* (14), 6687-6718.
(19) Copéret, C.; Comas-Vives, A.; Conley, M. P.; Estes, D. P.; Fedorov, A.; Mougel, V.; Nagae, H.; Núñez-Zarur, F.; Zhizhko, P. A. Surface Organometallic and Coordination Chemistry toward Single-Site Heterogeneous Catalysts: Strategies, Methods, Structures, and Activities. *Chem. Rev.* **2016**, *116* (2), 323-421.
(20) Samantaray, M. K.; D'Elia, V.; Pump, E.; Falivene, L.; Harb, M.; Ould Chikh, S.; Cavallo, L.; Basset, J.-M. The Comparison between Single Atom Catalysis and Surface Organometallic Catalysis. *Chem. Rev.* **2020**, *120* (2), 734-813.
(21) Samantaray, M. K.; Mishra, S. K.; Saidi, A.; Basset, J.-M. Surface organometallic chemistry: A sustainable approach in modern catalysis. *J. Organomet. Chem.* **2021**, *945*, 121864.
(22) Coperet, C. C−H Bond Activation and Organometallic Intermediates on Isolated Metal Centers on Oxide Surfaces. *Chem. Rev.* **2010**, *110* (2), 656-680.
(23) Brack, E.; Plodinec, M.; Willinger, M. G.; Coperet, C. Implications of Ga promotion and metal-oxide interface from tailored PtGa propane dehydrogenation catalysts supported on carbon. *Chem. Sci.* **2023**, *14* (44), 12739-12746.
(24) Alfke, J. L.; Tejeda-Serrano, M.; Phadke, S.; Tereshchenko, A.; Gani, T. Z. H.; Rochlitz, L.; Zhang, S. B. X. Y.; Lin, L.; Copéret, C.; Safonova, O. V. Boundary Conditions for Promotion versus Poisoning in Copper–Gallium-Based CO2-to-Methanol Hydrogenation Catalysts. *ACS Catal.* **2024**, 9166-9175.
(25) Li, X.; Wang, S.; Li, L.; Sun, Y.; Xie, Y. Progress and Perspective for In Situ Studies of CO2 Reduction. *J. Am. Chem. Soc.* **2020**, *142*, 9567−9581.
(26) Müller, H.; Seidel, W.; Görls, H. Zur Chemie des Dimesityleisens: VI. Die struktur von tetramesityldieisen. *J. Organomet. Chem.* **1993**, *445* (1), 133-136.
(27) Ehinger, C.; Zhou, X.; Candrian, M.; Docherty, S. R.; Pollitt, S.; Coperet, C. Group 10 Metal Allyl Amidinates: A Family of Readily Accessible and Stable Molecular Precursors to Generate Supported Nanoparticles. *JACS Au* **2023**, *3* (8), 2314-2322.
(28) Sot, P. Synthesis, characterization and reactivity of silica supported iron single sites for non-oxidative coupling of methane. ETH Zurich, Zurich, 2019.
(29) Chu, C. H.; Jonsson, E.; Auvinen, M.; Pesek, J. J.; Sandoval, J. E. A new approach for the preparation of a hydride-modified substrate used as an intermediate in the synthesis of surface-bonded materials. *Anal. Chem.* **1993**, *65* (6), 808-816.
(30) Portius, P.; Bühl, M.; George, M. W.; Grevels, F.-W.; Turner, J. J. Structure and Dynamics of Iron Pentacarbonyl. *Organometallics* **2019**, *38* (21), 4288-4297.
(31) Lyon, R. E. A Physical Basis for Kinetic Compensation. *J. Phys. Chem. A* **2023**, *127* (10), 2399-2406.
(32) Barrie, P. J. The mathematical origins of the kinetic compensation effect: 1. the effect of random experimental errors. *Phys. Chem. Chem. Phys.* **2012**, *14* (1), 318-326.
(33) Kattel, S.; Yan, B.; Chen, J. G.; Liu, P. CO2 hydrogenation on Pt, Pt/SiO2 and Pt/TiO2: Importance of synergy between Pt and oxide support. *J. Catal.* **2016**, *343*, 115-126.
(34) Mojet, B. L.; Ebbesen, S. D.; Lefferts, L. Light at the interface: the potential of attenuated total reflection infrared spectroscopy for understanding heterogeneous catalysis in water. *Chem. Soc. Rev.* **2010**, *39* (12), 4643-4655, 10.1039/C0CS00014K.

(35) Larmier, K.; Liao, W.-C.; Tada, S.; Lam, E.; Verel, R.; Bansode, A.; Urakawa, A.; Comas-Vives, A.; Copéret, C. CO2-to-Methanol Hydrogenation on Zirconia-Supported Copper Nanoparticles: Reaction Intermediates and the Role of the Metal–Support Interface. *Angew. Chem. Int. Ed.* **2017**, *56* (9), 2318-2323.
(36) Note: Room temperature CO-adsorption IR on PtFe@SiO2 presents two peaks for the same compound at 2025 cm-1 and 2005 cm-1 (Figure S). However, Berry-pseudo rotation of Fe(CO)5 at higher temperatures leads to the averaging of these features to a peak at 2013 cm-1. See Ref: (29).
(37) Meunier, F. C. Hydrogenation of CO and CO2: Contributions of IR operando studies. *Catal. Today* **2023**, *423*, 113863.
(38) Cao, L.; Liu, W.; Luo, Q.; Yin, R.; Wang, B.; Weissenrieder, J.; Soldemo, M.; Yan, H.; Lin, Y.; Sun, Z.; et al. Atomically dispersed iron hydroxide anchored on Pt for preferential oxidation of CO in H(2). *Nature* **2019**, *565* (7741), 631-635.